

New Structural Insights into Densely Assembled Reduced Graphene Oxide Membranes

Yang Cao, Zhiyuan Xiong, Fang Xia, George V. Franks, Lianhai Zu, Xiao Wang, Yvonne Hora, Stephen Mudie, Zijun He, Longbing Qu, Yanlu Xing, and Dan Li*

Densely assembled graphene-based membranes have attracted substantial interest for their widespread applications, such as compact capacitive energy storage, ion/molecular separation, gas barrier films, and flexible electronics. However, the multiscale structure of densely packed graphene membranes remains ambiguously understood. This article combines X-ray and light scattering techniques as well as dynamic electrosorption analysis to uncover the stacking structure of the densely stacked reduced graphene oxide (rGO) membranes. The membranes are produced by reducing graphene oxide (GO) membranes with hydrazine, during which the colloidal interactions between GO sheets are modulated by the electrolyte solution. In contrast to the common notion that direct reduction of densely assembled GO sheets in parallel tends to result in significant “graphitization”, this article unexpectedly discovers that the resultant densely packed rGO membrane can still retain the interconnected network nanochannels and show good capacitive performances. This inspires the development of a hierarchical structural model to describe the densely packed rGO membranes. This article further shows that the nanochannel network can be fine-tuned at the sub-nanometer level by tailoring the salt concentration and the reduction temperature to render exceptional volumetric capacitance and good rate performance for rGO membranes even with increased packing density.

require partial deoxygenation of GO to form reduced GO (rGO) to restore the π -conjugated structure and associated physical properties, such as high electrical conductivity and thermal stability.^[2] It has been widely demonstrated that in addition to the chemical composition, how the resultant rGO sheets are assembled or stacked in the final product can have substantial impacts on their properties and performance.^[3] The impacts become more significant when the packing density of the rGO assemblies reaches above 0.77 g cm^{-3} —corresponding to an average interlayer spacing of less than 1 nm (estimated based on assumption that the nanosheets are evenly separated with each other).^[4] It is thus required to carefully control the stacked structure of rGO, especially when the assembly is at the ultra-dense state. For example, dense rGO membranes with sub-nanometer (sub-nm) channels are promising to be applied for the separation of ions, gases, and solvents, but the separation application demands the precise control of interlayer spacing and defects

1. Introduction

Graphene oxide (GO), a partially oxidized derivative of graphene, has gained tremendous interest as an atom-thin building block to fabricate graphene-based bulk materials because of the ease of its scalable production from graphite and excellent solution processability.^[1] Many applications of GO-derived materials

of rGO sheets.^[5] Dense rGO membranes can also be used in energy storage and barrier films. The compact capacitive energy storage applications require the formation of a dense yet continuous ion transport network among rGO sheets.^[3b,4,6] Other applications that require exceptional thermal or mechanical performance and gas/liquid barrier applications can be achieved when the full graphitized restacking of rGO layers results.^[7]


Y. Cao, Z. Xiong, G. V. Franks, L. Zu, X. Wang, Z. He, L. Qu, D. Li
Department of Chemical Engineering
The University of Melbourne
Parkville, VIC 3010, Australia
E-mail: dan.li1@unimelb.edu.au

F. Xia
Harry Butler Institute
Murdoch University
Perth, WA 6150, Australia

Y. Hora
Monash X-Ray Platform
Monash University
Clayton, VIC 3800, Australia

S. Mudie
Small- and Wide-Angle X-ray Scattering Beamline
Australian Synchrotron
Clayton, VIC 3168, Australia

Y. Xing
School of Earth
Atmosphere and Environment
Monash University
Clayton, VIC 3800, Australia

 The ORCID identification number(s) for the author(s) of this article can be found under <https://doi.org/10.1002/adfm.202201535>.

© 2022 The Authors. Advanced Functional Materials published by Wiley-VCH GmbH. This is an open access article under the terms of the Creative Commons Attribution-NonCommercial License, which permits use, distribution and reproduction in any medium, provided the original work is properly cited and is not used for commercial purposes.

DOI: 10.1002/adfm.202201535

Dense rGO assemblies can be readily processed from rGO dispersions through solution processing techniques such as filtration.^[8] However, the processability, such as the concentration and long-term stability of the rGO dispersion, will be compromised due to the loss of hydrophilic oxygen groups. Additionally, rGO sheets in aqueous dispersion are found to be microscopically corrugated or crumpled over time, which could be detrimental to precisely controlling their stacking at the sub-nm level.^[9] Another strategy for fabricating dense rGO-based bulk materials involves the solution-phase processing GO into desired bulk assemblies such as membranes, foams, or fibers, followed by an additional reduction step to remove oxygen groups through chemical vapor, thermal, or laser reduction.^[1c,10] However, the deoxygenation process generally involves the generation of carbonaceous gases and strong in-plane strain in rGO sheets, which can have a drastic or even catastrophic influence on the packing structure and the structural integrity of the resultant rGO materials. For example, rapid heating of GO membranes through flash heating or laser scribing can cause explosive expansion of the membrane, leading to highly porous and loosely stacked structures.^[10b,11] The reduction of GO membranes with hydriodic acid vapor/solution can retain the dense structure of the membrane but eliminate the intrinsic sub-nm channels in GO sheets enabled by the oxygen-containing groups.^[12] The resultant rGO membranes are found to be considerably “graphitized” and become impermeable to water, helium, and ions, completely losing the capability for the selective separation of molecules.^[13] Thus, the successful adoption of the latter strategy in the future will largely depend on whether the stacking structure of rGO sheets can be well controlled at will.^[14] Hence there are strong incentives to develop new approaches to characterize how the stacking behavior of GO nanosheets evolves during the deoxygenation process and to precisely modulate the stacked features to realize desired architectures in a controllable manner.

A variety of techniques have been developed to characterize the stacking and pore formation of rGO assemblies. For example, a penetration test with various gas molecules has long been conducted to characterize porous carbon.^[11b,15] However, the gas adsorption is often considered not suitable for probing the porous structure of microporous carbon, because this measurement would underestimate the surface area of micropores (especially <0.7 nm) and overestimate that of larger pores.^[16] This penetration measurement is also likely to disturb the porous structure as it usually requires a pre-treatment of the sample, such as degassing, drying, and annealing.^[9c] X-ray diffraction (XRD) is widely used to characterize the interlayer stacking of the dense rGO assemblies but is limited in scope to characterizing only well-crystallized regions at the nm scale.^[4] As the performances of rGO assemblies depend on not only the average pore size but also pore size distribution, as well as the pore connectivity,^[17] it is essential to characterize their structure across a full spectrum of length scales. However, the previous characterization of dense rGO assemblies was mainly focused on their average interlayer spacing within the nm scale; the structural variance at the sub-nm scale and other features at mesoscale (2–50 nm) or above remain poorly understood.

In this work, we used the densely packed multilayered GO membranes reduced in aqueous hydrazine solutions as a model system to study the stacking structure of rGO nanosheets

across multiple length scales. We combined X-ray and light scattering techniques with the electrosorption characterization to shed a light on the stacking and pore formation of individual nanosheets during the membrane reduction across multiple length scales. Additionally, the laminar membrane structure enables us to estimate its interlayer porous structure by the total thickness of the membrane. Our initial intuition was that the close and parallel stacking of GO sheets in the membrane should favor the formation of graphite-like structures after the deoxygenation because the π - π interactions between rGO sheets should dominate, as with the case observed in the reduction of GO membranes by hydriodic acid vapor.^[13] Instead, our experiments revealed that even in the ultra-dense (>1.5 g cm⁻³) rGO membrane, complete “graphitization” does not occur but a continuous nanochannel network can be retained after the reduction. Accordingly, we proposed a hierarchical structure model to describe how nanochannels, graphitized clusters, and relatively large voids co-exist in the dense rGO membranes through an interconnected hierarchical structure. A hierarchical structure has been reported for the low-density mesoporous rGO-based membranes with pores ranging from micrometer to nanometer scale,^[18] nevertheless, we demonstrate that even the ultra-dense rGO membranes still contain the porosity in the hierarchy. More importantly, we show that the hierarchical structure of the resultant dense yet porous rGO membranes can be fine-tuned by using salt concentration to modulate their colloidal interactions to offer an exceptional volumetric capacitance in aqueous electrolytes.

2. Results and Discussion

2.1. “Unexpected” Observation with GO Membranes Reduced in Electrolyte Solutions

The GO membranes are known to swell and disintegrate in water or basic solutions due to the inter-sheet electrical double layer (EDL) repulsion among the ionizable oxygen-containing groups.^[8,19] To maintain the structural integrity of GO membranes during the wet-chemical reduction, we added NaCl to screen the inter-sheet EDL interactions. As illustrated in **Figure 1a**, the vacuum-filtrated GO membranes (the dimensions of the GO flakes used in this work are shown in **Figure S1**, Supporting Information) were chemically reduced by N₂H₄ in aqueous NaCl solution first at 30 °C for 24 h and then heated to 90 °C for 1 h (more details in Experimental Section). Compared to the conventional preparation of rGO dispersion from a GO colloid in which GO sheets are well separated,^[8] the GO sheets are already spatially restricted in the membrane. We thus refer to the as-reduced product as the spatially restricted rGO membranes (denoted as R-rGO). Moreover, we found that when the NaCl concentration is higher than 0.3 M, the R-rGO membranes can retain their shape during the chemical reduction process (**Figure S2**, Supporting Information). Scanning electron microscope (SEM) analysis of the dried membrane reveals a densely laminated structure as expected (**Figure 1b**). For comparison, we also prepared rGO membranes via direct reduction of the GO dispersion (0.5 mg mL⁻¹) in hydrazine and followed by vacuum filtration (**Figure 1a**) using the method reported.^[8] Those membranes prepared from the rGO nanosheets freely

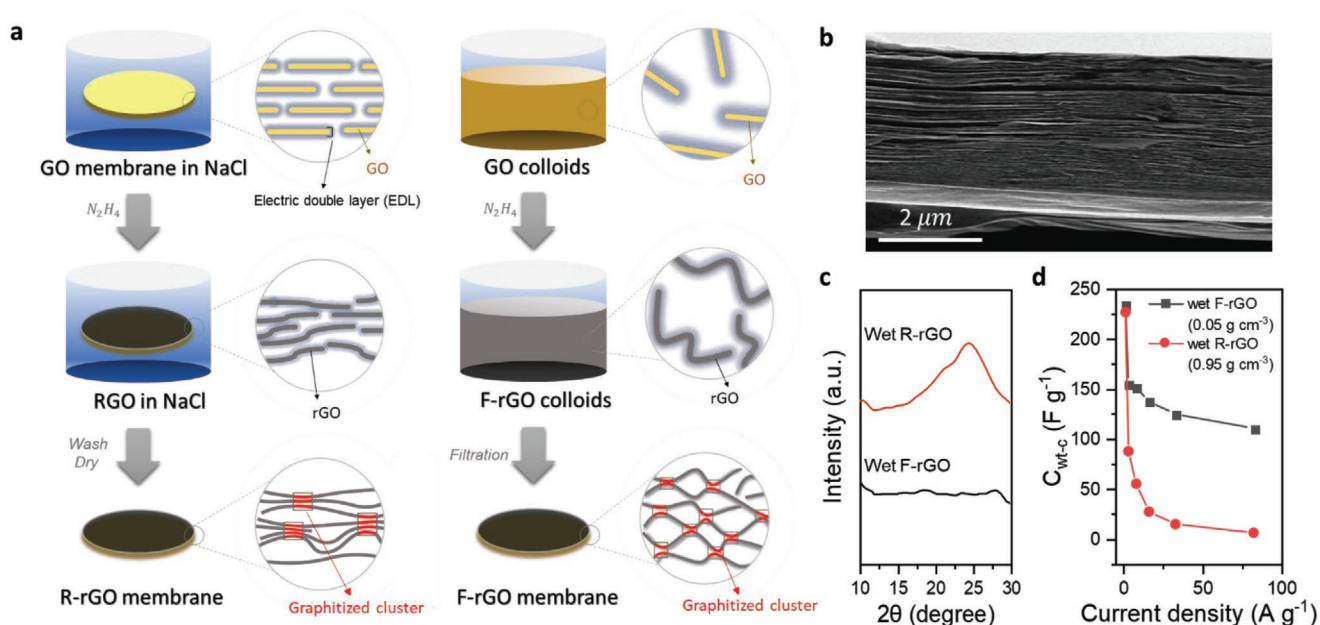


Figure 1. Preparation and characterization of spatially restricted-reduced GO (R-rGO) in aqueous NaCl solution. a) Schematic illustrating the preparation procedure of R-rGO membrane and freely reduced GO (F-rGO) membrane. b) SEM images of the cross-section of an R-rGO membrane reduced from 0.3 M NaCl. c) XRD spectra of the wet R-rGO reduced from 0.3 M NaCl in comparison with the rGO hydrogel membrane prepared by filtration of F-rGO colloids. d) Electrosorption characterization of R-rGO membrane prepared from 0.3 M NaCl in 1.0 M H₂SO₄ in comparison with F-rGO membranes. The gravimetric capacitances (C_{wt-c}) of the membranes are plotted against various charging current densities. The mass loading of those membranes is $\approx 1.0 \text{ mg cm}^{-2}$.

suspended in an aqueous solution are denoted as the freely reduced GO (F-rGO) membrane.

The stacking state of rGO nanosheets in the wet membranes was analyzed with XRD. As shown in Figure 1c, the wet F-rGO membrane shows no detectable diffraction peak, which is consistent with previous studies that the rGO nanosheets are largely separated to form an open porous network.^[4,20] In contrast, the wet R-rGO membrane with a similar C/O ratio to the F-rGO membrane (Table S1, Supporting Information) exhibits a distinct diffraction peak at $\approx 25^\circ$, corresponding to an interlayer spacing of $\approx 0.36 \text{ nm}$. This result suggests that the graphitization-like stacking already exists in R-rGO membranes, and this type of stacking should occur during the chemical reduction process as the original GO membrane does not show any graphitization (Figure S3, Supporting Information).

We further evaluated the pore structure of the two types of membranes by comparing their ion electrosorption behaviors.^[21] The actual pore structure is retained and can be measured in this electrosorption method as it does not require any sample pre-treatment such as drying, annealing, degassing required for the Brunauer–Emmett–Teller (BET) test,^[9c,16a] which can alter the pore structure of the material. We found that the gravimetric capacitance (C_{wt-c}) of the wet R-rGO membrane prepared in the presence of 0.3 M NaCl (a.q.) is much lower than that of the wet F-rGO membrane at high charging rates ($>2.5 \text{ A g}^{-1}$, Figure 1d, measured in 1.0 M H₂SO₄ electrolyte). However, at a relatively low charging rate (1.0 A g^{-1}), when the influence of ion kinetics is insignificant, both the membranes give rise to a similar capacitance, indicating comparable ion-accessible pore surface area. This result suggests that the R-rGO membrane is still very porous in the wet state

even though XRD shows the occurrence of graphitization (Figure 1c). This appears contradictory to the common notion that the graphene sheets have a strong tendency to restack into the graphite-like structure in the aqueous environment due to their high hydrophobicity,^[8] especially when the presence of the electrolyte (e.g., NaCl) in the solution can further screen the inter-sheet EDL repulsion.

We have previously found that drying the F-rGO hydrogel membrane can lead to a significant shrinkage of the interlayer distance from ≈ 10 to $\approx 0.6 \text{ nm}$ and partial graphitization as evidenced by the appearance of the diffraction peak at $\approx 25^\circ$ in its XRD pattern.^[20] To test if the drying process could cause the restacking of rGO sheets in the R-rGO membrane, we dried the R-rGO membrane using vacuum filtration^[20] for further characterization (samples mentioned in the following section are all in a dried state unless specified). Interestingly, we observed that the dried R-rGO shows higher C_{wt-c} than that of dried F-rGO (195 vs 150 F g^{-1}) in H₂SO₄ electrolyte at a current density of 1.0 A g^{-1} despite that the packing density of rGO nanosheets in R-rGO is much higher than the one in F-rGO (1.34 vs 1.17 g cm^{-3}) in the electrolyte solution (Figure S4a, Supporting Information), indicating that the dried R-rGO is still porous and even contains a higher ion accessible surface area than F-rGO. Besides, the quasi-rectangular shape of the cyclic voltammetry (CV) curve also confirms the porous structure of the R-rGO membrane (Figure S4b, Supporting Information). The XRD and electrosorption results suggest that the R-rGO membranes contain both graphitized clusters and porous regions. The widely used structural model of GO and rGO membranes in which individual sheets are evenly distributed along the laminar direction (see the rightmost panel conventional model in

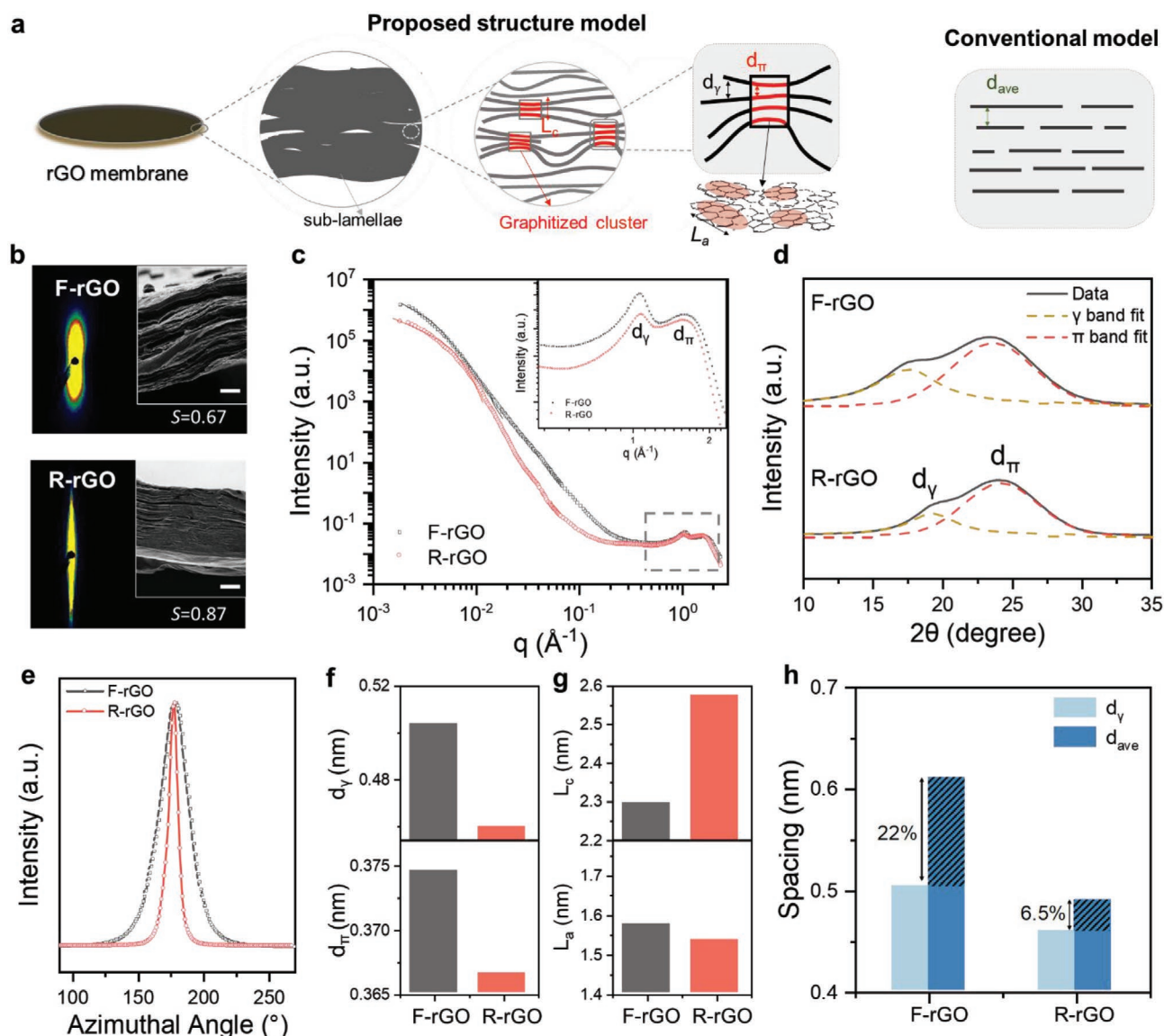


Figure 2. Characterization of the structure of R-rGO membrane. a) Schematic illustration of the hierarchical structure model of rGO membrane and comparison to the conventional structure model. The rGO membrane is formed by the network of staggered sub-lamellae. Each sub-lamellae consists of the laminated porous regions crosslinked by graphitized clusters, which were assembled by the closely packed micro-corrugated nanosheets. Stacking height (L_c), interlayer spacing (d_π) are the key variables to describe the graphitized clusters. Domain size (L_a) describes the average size of aromatic domains in the individual graphene nanosheet. Interlayer spacing of sub-nm channel (d_γ) probed by XRD, average interlayer spacing (d_{ave}) estimated by its relative density to graphite, spacing of amorphous/large voids (d_{void}) is the key variables to describe the hierarchical porous size of graphene membranes. b) 2D SAXS pattern from the through-the-edge direction with an accessible range of scattering vector, q , of 0.002 \AA^{-1} to 0.1 \AA^{-1} . Orientational distribution coefficient, S , is calculated by Hermans' distribution function. Insets are the SEM images of the cross-section of the rGO membrane. Scale bars are $1 \mu\text{m}$. c) 1D scattering curves plotted as intensity (I) as a function of scattering vector (q). The intensity is averaged with a mask on the stretched direction of the through-the-edge sample (See Figure S5, Supporting Information). Inset is the magnification of the high- q range. d) XRD spectra and the Lorentz fitting of the XRD patterns with γ band ($\approx 17^\circ$) and π band ($\approx 25^\circ$). e) Plot of the azimuthal dependence of the scattering intensity obtained from the 2D scattering pattern (b). f) Plot of d_π and d_γ characterized by XRD spectra. g) L_a and L_c calculated by the Sheerer equation and Lucchese model, respectively. h) Comparison of d_{ave} and d_γ . The discrepancy of these two types of interlayer spacing is presented in a percentage calculated by $\frac{d_{ave} - d_\gamma}{d_\gamma}$. This value estimates the amount of large voids that exist in the membrane.

Figure 2a for a schematic) cannot accurately describe the structure of our R-rGO membranes. Instead, we propose a structural model of porous regions of rGO sheets between graphitized clusters (the left panels of Figure 2a), as described in the next section.

2.2. Multiscale Characterization and a New Structure Model for rGO Membranes

We performed synchrotron-based small-angle X-ray scattering (SAXS) to investigate the stacking structure of the membranes

ranging from sub-nm to μm scale. The membranes were characterized by scattering through the surface and the edge, respectively (Figure S5, Supporting Information). Both F-rGO and R-rGO exhibit the anisotropic pattern through the edge direction but isotropic scattering pattern through the surface direction (Figure S5, Supporting Information) owing to the oriented alignment of rGO nanosheets along its plane direction. Both the $I-q$ curves of R-rGO and F-rGO probed through the edge direction show several features (peaks and/or humps) at different q -regions (Figure 2c), which can be used to extract the structural information of the stacking from different length scales. In particular, two distinct peaks are found over the high q region ($q > 0.3 \text{ \AA}^{-1}$), indicating two correlation distances ($d = \frac{2\pi}{q}$) exist between the stacked rGO nanosheets at the sub-nm level. A similar structure is also observed in amorphous porous carbon (e.g., pyrocarbon and coals)^[22] containing pores and graphitized clusters together. At the low q region ($q < 0.02 \text{ \AA}^{-1}$), a weak hump with a correlation distance of 30–200 nm appeared, most likely due to the gaps formed between the sub-lamellae, an intermediate feature composed of a group of rGO nanosheets stacked in a planar manner. The existence of the sub-lamellae can be further confirmed by the striations on the SEM images (Figure 2b insets). This observation agrees with the previous studies about the formation of sub-lamellae in the GO membranes.^[23] The spaces in-between the staggered sub-lamellae could contribute to another group of mesopores (d_{void}) which has been shown in some studies.^[23a]

Based on the above results, we propose a hierarchical structure model for F-rGO and R-rGO membranes in which the co-existence of graphitized domains, laminated porous regions, and relatively large voids in the membrane can be reflected. As shown in Figure 2a, i) the micro-corrugated rGO sheets are first stacked to form individual sub-lamellae, in which individual rGO sheets stack to form graphitized clusters with an interlayer distance of $\approx 0.37 \text{ nm}$ (d_{π}) and ordered nanochannel regions with a feature spacing below 1.0 nm (d_{γ}). The nanochannel regions are largely interconnected (as evidenced by the electrosorption results). The rGO sheets that surround the nanochannels are also physically linked together through the graphitized domains to maintain the structural integrity; ii) the sub-lamellae are staggered to construct the integrated membrane, in which the large pores (d_{voids}) with the size of 30–200 nm are formed in between the individual lamellae. The structural characterizations across multiple length scales described below provide more insights into the proposed structural model.

The XRD results can be used to quantitatively illustrate the stacking structure at the nanoscale by fitting with the two-peak model^[24] (Figure 2d), in which i) γ band ($2\theta = \approx 17^\circ$) represents the ordered porous region with the average spacing of d_{γ} , and ii) π band ($2\theta = \approx 25^\circ$) stands for the nano-graphitized clusters with the average spacing of d_{π} and the dimension of stacking height (L_c) (Figure 2a). The fitting results show that the R-rGO membrane has a slightly narrower d_{γ} ($\approx 0.46 \text{ nm}$) compared to that of F-rGO ($\approx 0.50 \text{ nm}$) (Figure 2f), demonstrating rGO nanosheets reduced in the electrolyte solution are prone to more densely stacked in the porous region. This result is in agreement with the density profile (1.58 g cm^{-3} for R-rGO compared to 1.23 g cm^{-3} for F-rGO). The aromatic domain

size (L_a) of the R-rGO layers and F-rGO layers are nearly the same ($\approx 1.55 \text{ nm}$) (Figure 2g), which means that these two types of reduction routes do not result in significant differences in the graphitization of a single nanosheet. This phenomenon could explain why R-rGO and F-rGO end up with similar C/O . Although they have similar L_a , R-rGO exhibits slightly thicker graphitized clusters L_c ($\approx 2.57 \text{ nm}$) compared to that of F-rGO ($\approx 2.30 \text{ nm}$), suggesting the increased graphitized crystallite size along the laminated stacking direction (Figure 2g).

We further compared the average interlayer spacing (d_{ave}) and the spacing in the laminated porous region (d_{γ}) to estimate the contribution from large voids (d_{void}). Because these rGO membranes have a laminar structure, the d_{ave} can be obtained by the relative density to graphite (Equations (1) and (2)).^[4] This value represents the average features of overall pore information, including spacing in large voids, ordered porous region, and graphitized stacking region (d_{void} , d_{γ} , and d_{π} , respectively). Thus, the relative volume of the large voids in these membranes can be estimated by the increased portion of d_{ave} compared to d_{γ} . Our results (Figure 2h) show that d_{ave} exceeds d_{γ} for both R-rGO and F-rGO, implying the existence of large voids in both membranes. The decreased discrepancy between d_{ave} and d_{γ} for R-rGO (6.5%) compared to F-rGO (22%) indicates the less total volume of voids formed in R-rGO. Additionally, R-rGO shows a relatively constrictive hump compared to F-rGO in the low q region ($q < 0.01 \text{ \AA}^{-1}$) of the SAXS patterns (Figure 2c), indicative of narrower size distribution of the large voids through the membrane.

The less broadening of the SAXS scattering pattern (Figure 2b) suggests that R-rGO has a higher degree of sheet alignment and narrower pore size distribution compared to F-rGO. This effect can also be demonstrated by the narrow peak width of R-rGO in the azimuthal intensity profile (Figure 2e), which correlates to a higher orientational distribution coefficient (S)^[25] than F-rGO (0.87 vs 0.67) (Figure 2b). The Raman analysis also indicates the less amorphous region and enhanced structural ordering in R-rGO (Figure S6, Supporting Information). The higher stacking ordering and narrow pore size distribution of R-rGO compared to F-rGO is presumably a result of the fewer in-plane corrugations implied by the smaller value of the surface fractal dimension (D_s)^[26] obtained from the scattering curve measured through the surface of the membrane (2.86 for R-rGO and 2.93 for F-rGO, Figure S7, Supporting Information).

The above analysis indicates that although R-rGO exhibits a denser and more ordered stacking structure than F-rGO, the majority of sheets remains separated at the sub-nm scale and form hierarchical pores. The resistance to complete graphitization could be ascribed to the unique stacking behavior of the individual rGO sheets during the reduction of GO membranes. According to the XRD patterns of R-rGO in the wet and dry states (Figures 1c and 2d), the restacking of R-rGO was found to have already occurred during the reduction. Due to the multiple in-plane sp^2 and sp^3 domains distributed throughout the nanosheets, the rGO would have several graphitized nucleation sites in overlapped sp^2 regions of two stacked nanosheets during the reduction.^[2a] In this case, as the graphitized nucleus grows, there would be some stacking faults (curving, folding)^[6,27] forming between the graphitized clusters, which

result in the formation of the majority of the pores. Besides, according to chemistry characterization (Table S1, Supporting Information), there are still some residual oxygen-containing groups on the nanosheets, which could also contribute to the pore formation.

2.3. Tuning the Hierarchical Structure of R-rGO Membranes

We have previously found that the colloidal interaction plays a crucial role in keeping the resultant GO sheets apart for the formation of a stable rGO dispersion without the use of any surfactants.^[8] We were curious whether the colloidal interactions could affect the structural evolution of GO membranes during the reduction. Hence, we modulated the electrolyte concentration involved in the reduction process and conducted a series of experiments to examine whether the hierarchical structure of the rGO membranes can be controlled by the synthesis conditions. For simplicity, the membranes reduced in different electrolyte concentrations are denoted as R-rGO-*X* (*X* represents the concentration of NaCl solution in molar). Two-step reductions are conducted to make sure a gentle reduction reaction for the GO membrane (see Experimental Section). Interestingly, we found that the electrolyte concentration has a significant impact on the stacking structure of R-rGO sheets after being initially reduced at 30 °C. This could be attributed

to the influence of electrolyte concentration on the inter-sheet interactions. For the unreduced GO membrane, its interlayer distance (d_{ave}) decreases with the increase of the electrolyte concentration (Figure 3a) because an increased electrolyte concentration would further screen the EDL repulsion between GO sheets (Equation (S1), Supporting Information).^[28] As expected, the d_{ave} of GO membranes shows a roughly linear relationship with the Debye length (κ^{-1}) (Table S2 and Figures S8 and S9, Supporting Information), which is in agreement with previous studies on the swelling of clays in the electrolyte.^[29] After reduction, we observe that the electrolyte concentration leads to both decreased d_{π} (from 0.37 to 0.35 nm) and d_{γ} (from 0.52 to 0.41 nm) for F-rGO to R-rGO-0.5 (Figure 3b), consistent with their increased density (Figure S10, Supporting Information) and the observation from the SAXS profile at high-*q* region (Figure S11a, Supporting Information). Meanwhile, the increased electrolyte concentration facilitates the growth of graphitic clusters mainly in the stacking direction with L_c increasing from 2.1 to 5.2 nm (Figure 3d). These suggest that R-rGO nanosheets reduced in solutions with higher electrolyte concentration tend to stack with the neighboring nanosheets, forming larger and denser graphitized clusters. Furthermore, the decreased ratio of the π band to γ band indicates that lesser graphitized crystalline fraction for the resultant membranes with the increasing electrolyte concentration (Figure 3b). The smaller graphitized contents combined with the increasing

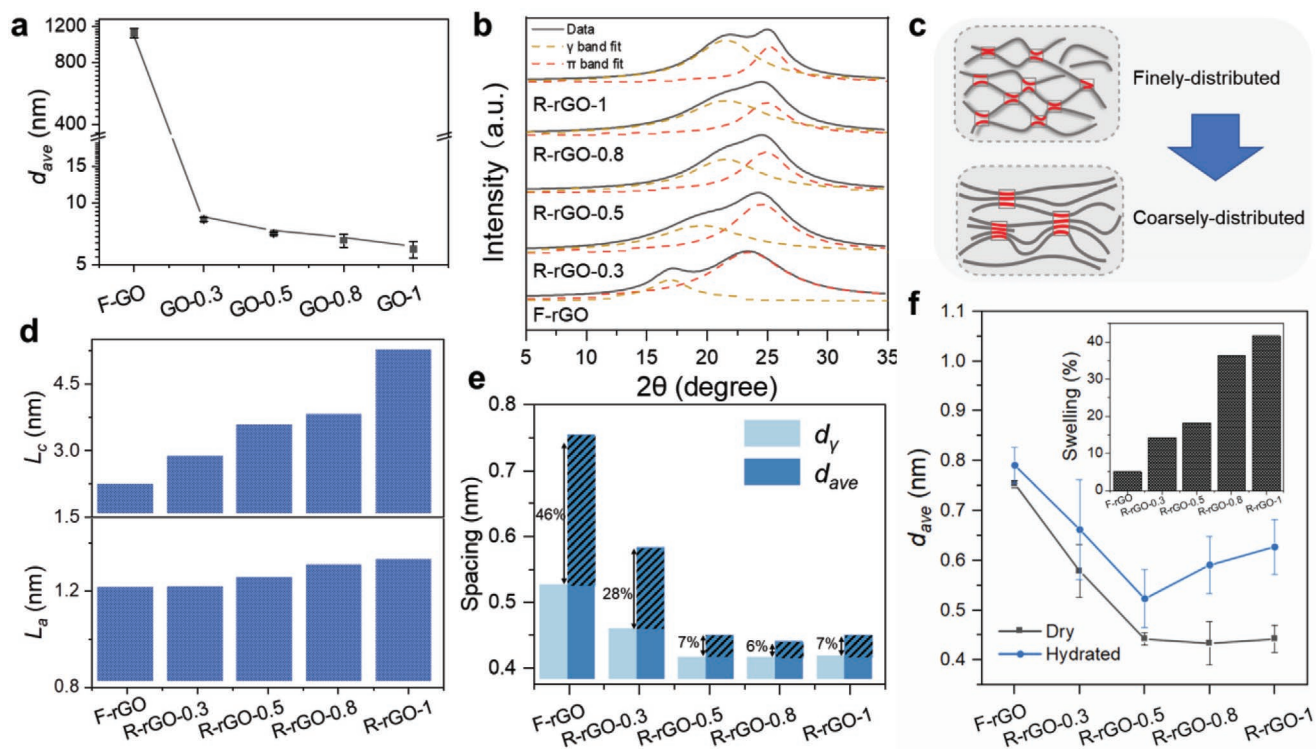


Figure 3. The structure of R-rGO membranes obtained from different concentrations of electrolytes after being reduced at 30 °C. a) The d_{ave} of F-GO (0.5 mg mL⁻¹) and GO-*X* (*X* represents the concentration of NaCl in mole) (before reduction) by concentration and thickness, respectively. b) XRD patterns and the Lorentz fitting of the XRD patterns with γ band ($\approx 17^\circ$) and π band ($\approx 15^\circ$). c) Schematic drawing of the rGO membrane with the fine-tuned nanostructure. Top: rGO membrane with finely distributed graphitized cluster (low salt concentration). Bottom: rGO membrane with coarsely distributed graphitized cluster (high salt concentration). d) Plot of L_a and L_c . e) Comparison of d_{ave} and d_{γ} . f) Comparison of the d_{ave} in the dry and solvated state. Inset is the evolution of the swelling ratio of membrane placed in the solvated state and dry state.

crystalline size suggest that a more coarsely distributed graphitic cluster was formed in the R-rGO membrane reduced at a higher concentration of electrolyte (Figure 3c). Given that the graphitized clusters can keep the membrane stability by the strong Van der Waals interactions^[30] and those membranes have similar C/O (Tables S3 and S4 and Figure S12, Supporting Information), such coarsely distributed graphitic structure could be also reflected by significantly enhanced swelling ratio of membranes in an aqueous environment (from 5% to 42% for F-rGO to R-rGO-1) (Figure 3f). Additionally, we found that fewer voids were formed with the increasing electrolyte concentration from F-rGO to R-rGO-0.5 and above, as suggested by the decreased discrepancies between the d_{ave} and d_{γ} (from 46% to 7%) (Figure 2e). The fewer voids formed in the higher electrolyte concentration are consistent with the smoother surface morphology inferred by the decreased D_s (Figure S11b, Supporting Information) and smaller in-plane strain indicated by Raman (Figure S13, Supporting Information).

However, the influence of electrolyte concentration on the porous structure of R-rGO membranes was insignificant when the membranes were further treated at 90 °C (Figures S14–S16, Supporting Information). After this high-temperature treatment, the d_{π} and d_{γ} remained at ≈ 0.37 and ≈ 0.47 nm, respectively, and the L_c was kept at ≈ 2.5 nm for all R-rGO membranes reduced from different concentrations of salts (Figure S15, Supporting Information). The minor effect of electrolyte concentration on the stacking structure after high-temperature treatment can also be confirmed by the similar electrosorption behavior of R-rGO membranes (Figure S16, Supporting Information). This appears to indicate that the level of micro-corrugation of individual rGO sheets reduced at 90 °C is overwhelmed by the thermal stresses.^[9a] These results suggest that the stacking of rGO nanosheets during the reduction process is a result of dynamic competition between non-covalent interactions mediated by the electrolyte and the disturbance introduced by the high-temperature reduction. Besides, there is a distinct structure variance between F-rGO and R-rGO, no matter whether it is reduced at 30 °C or further treated at 90 °C. This observation shows that the sequence of processing is essential for the stacking behavior of rGO nanosheets, and the direct reduction from GO membranes provides additional tunability of the pore structure at the sub-nm scale, which is difficult from the F-rGO.

2.4. Implications for Future Applications of R-rGO Membranes

It is well recognized that tuning the architectures of graphene-based assemblies, especially for the ultra-dense graphene materials, is important as it is the key determinant to the performance of many applications, such as compact energy storage,^[6] ion separation,^[31] water desalination,^[32] and bioelectronics.^[33] Note that previous studies on controlling the porous structure of rGO membranes predominantly focus on tailoring the average interlayer spacing^[6,16b] and in-plane pores.^[34] Here, we demonstrate that the porous structure of the R-rGO membrane is hierarchically distributed and can be fine-tuned at the sub-nm scale. This new understanding and the delicate control of the hierarchical structures provide more opportunities for tailoring the membrane functionalities than previous strategies.

One demonstration of the R-rGO with fine-tuned nanostructure presented here is their unique capacitive behaviors. We measured their electrochemical performance in the form of an asymmetric supercapacitor in 1.0 M H₂SO₄. According to the CV curves (Figure 4a,b), all samples show a nearly rectangular shape, indicating a typical EDL capacitance of the rGO membranes. Despite the slightly lower C/O ratios of R-rGO-0.8 and R-rGO-1 compared to others (Table S3, Supporting Information), the remaining oxygen groups did not trigger detectable redox reactions during the charging and discharging process. It is found that as the current density increases, the C_{wt-c} for all R-rGO membranes is higher than that of the F-rGO membranes (Figure 4d). In particular, R-rGO-0.8 shows the highest C_{wt-c} in a broad range of current density from 1.0 A g⁻¹ (236 F g⁻¹) to 150 A g⁻¹ (70 F g⁻¹). Meanwhile, the density of rGO membranes in the 1.0 M H₂SO₄ electrolyte increases from F-rGO (0.96 g cm⁻³) to R-rGO-0.5 (1.45 g cm⁻³) and drops to R-rGO-1 (1.21 g cm⁻³). When both C_{wt-c} and density are considered, R-rGO-0.8 still shows exceptional volumetric capacitance (C_{vol}) over 300 F cm⁻³ at 1.0 A g⁻¹ (Figure 4e), which is quite competitive compared with the EDL capacitance of other porous carbon electrodes in 1.0 M H₂SO₄ (Table S5, Supporting Information). After 10 000 charging/discharging cycles, R-rGO-0.8 membranes-based supercapacitors show coulombic efficiency above 97% and capacitance retention above 95% (Figure 4g), demonstrating good electrochemical stability.

The Nyquist plot further demonstrates the exceptional rate capability of R-rGO-0.8 and reveals their ion transport behaviors (Figure 4c). Specifically, the ending of the Warburg region (a line at $\approx 45^\circ$) pushes to a higher frequency from F-rGO to R-rGO-0.8, indicating more efficient ion transportation. This observation also can be confirmed by the EIS fitting showing that the ion transfer resistance (R_{ti}) decreases from 31.4 to 14.7 Ω for F-rGO to R-rGO-0.8 and then increases to 22.9 Ω for R-rGO-1, respectively (Figure S17 and Table S6, Supporting Information).

The observation that R-rGO membranes with higher density show better rate performance is counterintuitive and contrasts with the previous studies that rGO membranes with higher packing density usually are less ideal for ion transportation during charging and discharging.^[4,6,35] According to the sheet resistivity profile (Figure S18, Supporting Information) and EIS fitting results (Table S6, Supporting Information), the increased rate performances of R-rGO membranes should be attributed to the ion transportation pathway which is associated with the fine-tuned nanostructure, rather than the electron transfer. Our characterization reveals a structure of dense packing with the coarsely distributed graphitic clusters for R-rGO membranes prepared from a higher concentration of NaCl solutions (Figure 3). The coarsely distributed crosslinker potentially contributes to improved pore connectivity that is less impeded for ion transportation, which can be theoretically supported by the decreased pore tortuosity factors (τ) calculated from the Tau-Factor developed by Copper et al. (Figure S19, Supporting Information).^[36] It is therefore essential to thoroughly understand the stacking structure of rGO membranes at multiple length scales for establishing the proper structure-property relationship and for the rational design of the nanostructure to achieve better performances in future applications.

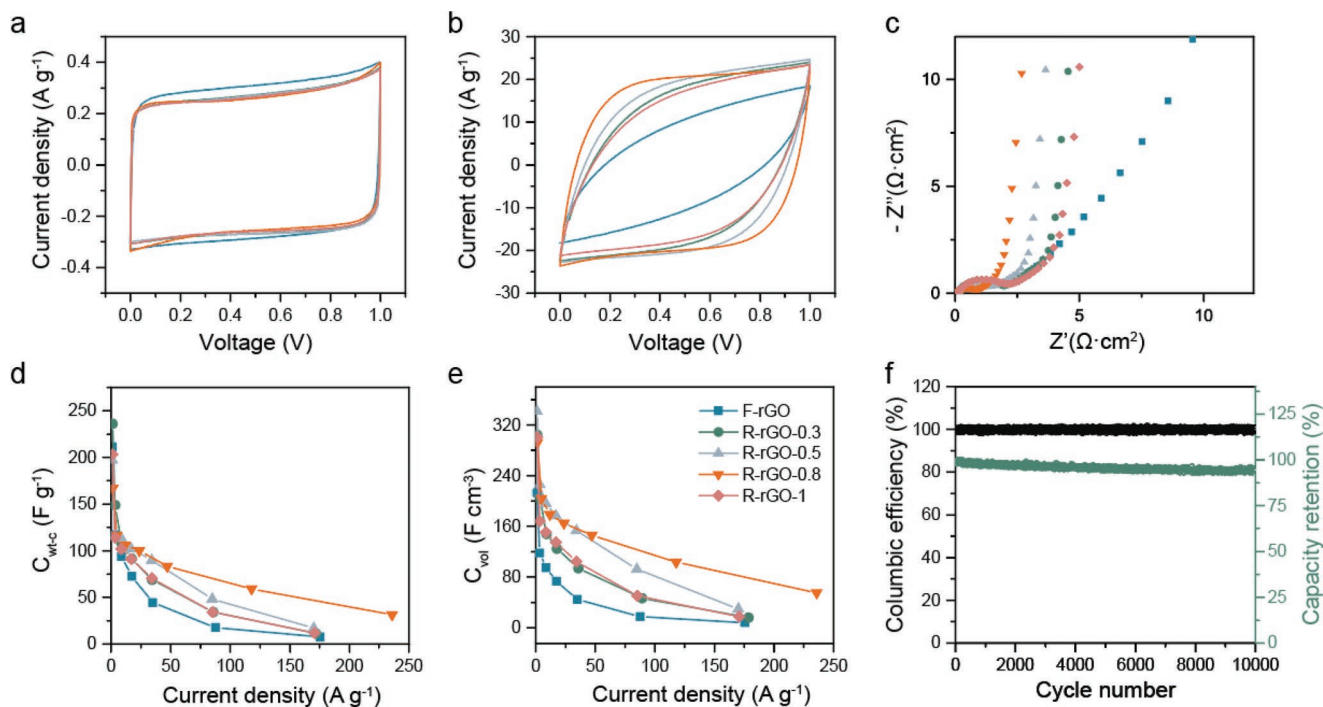


Figure 4. Electrochemical characterization of R-rGO membrane-based supercapacitors in 1.0 M H₂SO₄. CV curves at a scan rate of a) 5 mV s⁻¹ and b) 500 mV s⁻¹. c) Comparison of Nyquist plots. Plots of d) C_{wt,c} and e) volumetric capacitances (C_{vol}) as a function of current density. f) Cycling stability of the R-rGO-0.8 at a current density of 10 A g⁻¹. The mass loading of those membranes is 1.0 mg cm⁻². The symbols in all the panels are the same as indicated in panel (e).

3. Conclusion

The structural features of closely arranged rGO nanosheets were investigated in this study at multiple length scales with the model system of GO membrane reduced by hydrazine in electrolytes. We found that direct reduction of restricted GO membranes in NaCl solutions did not lead to substantial graphitization, but instead, the materials retained interconnected nanochannels. We further fine-tuned such structure at the sub-nm scale via controlling NaCl concentration at low reduction temperature. With this control, a dense yet interconnected porous graphene membrane, which exhibits high volumetric capacitance and rate capability, can be prepared. This new observation is potentially attributed to the coarsely distributed graphitized clusters, which less impede ion transport. Our study discovers the influence of a composite network of graphitized clusters and porous regions on the ion transportation behaviors in the rGO membranes, demonstrating that an accurate structure model is vital for understanding the real structure–property relationship. The co-existence of the graphitized stacking and pore formation can be prevalent in many other bottom-up manufactured graphene or other 2D materials assemblies, which, however, could be often overlooked by the previous studies from the oversimplified conventional structure model. This study provides a new paradigm to describe the structure of dense rGO assemblies and reveals the hidden importance of nanotexture in ion transportation properties. We suggest the new findings can help reassess the relationship between nanostructure and the ion transportation properties and rationally design the nanostructure for many other applications.

4. Experimental Section

Preparation of R-rGO Membrane: GO aqueous dispersion was prepared by a modified Hummers' method.^[37] 9.0 mg mL⁻¹ GO dispersion was diluted in Milli-Q water to yield a concentration of 0.5 mg mL⁻¹ and then sonicated for 30 min at the amplitude of 30% of the maximum power (500 W) in the ice-water bath. The GO membrane was fabricated by filtration of 30 mL GO dispersion on a polycarbonate (47 mm, PC 4700, Isopore) substrate with a pore size of 0.1 μm for 24 h to make a dried membrane. The prepared GO membrane was then cut into small pieces (diameter of 0.6 cm) and placed in 5 mL NaCl solution (1.0, 0.8, 0.5, and 0.3 M) for 4 h to allow the membrane to swell in the electrolyte fully. Then, hydrazine (N₂H₄, 35 wt%) was added to the electrolyte at the volume ratio of V_{N₂H₄} : V_{NaCl(aq.)} = 1 : 50. The reduction was conducted under 30 °C for 24 h first to prevent the membrane from disintegration caused by severe reduction at high temperature and then further reduced under 90 °C for 1 h to fully remove the residual functional groups. After that, the R-rGO membrane was thoroughly washed with Milli-Q water for 2 days to remove NaCl and dried by the filtration set.

Preparation of F-rGO Membrane: 0.5 mg mL⁻¹ GO dispersions (30 mL) were used to prepare rGO colloids. The pH of GO colloids was adjusted to ≈10 by adding ammonia solution (NH₃·H₂O, 30 wt%) before reduction, followed by adding the hydrazine (N₂H₄, 35 wt%) at the volume ratio of V_{N₂H₄} : V_{GO(aq.)} = 1:50. The colloids were kept at 30 °C for 24 h. The as-prepared rGO colloids were used to fabricate the rGO membrane. Filtration of 30 mL rGO colloids on a polycarbonate (PC 4700, Isopore) substrate with a pore size of 0.1 μm for 24 h makes the dried membrane. Then the filtrated membrane was cut into small pieces with a diameter of 0.6 cm for characterization.

Chemistry of rGO Membrane: X-ray photoelectron spectroscopy (XPS) was conducted by Nexsa Surface Analysis System with monochromatic Al Kα X-rays (1486.6 eV) at 72 W (6 mA and 12 kV, 400 × 800 μm² spot) as the incident radiation. The survey spectra were recorded with a 1.0 eV

step size, 10 ms dwell time, and a 150 eV pass energy. All high-resolution spectra were measured with a 0.1 eV step size, 50 ms dwell time, and a 150 eV pass energy. The analysis chamber base pressure was better than 5.0×10^{-9} mbar, and surface charging was controlled using a low-energy dual-beam (ion and electron) flood gun. Before scanning, every sample was etched using a 2000 eV ion beam for 45 s to make sure that the deeper section of the rGO membranes was probed. The final spectra were processed using CasaXPS (V5.99) and averaged using five-point scans.

Initial Interlayer Spacing of GO Membrane in NaCl with Different Concentrations: An optical microscope was used to in situ probe the thickness variance of GO membrane solvated in NaCl with different concentrations. The membrane was settled in a transparent container with the cross-section face vertically to the light path. Then, 3.0 mL NaCl aqueous solution (0.3 M) was added to the container. The swelled membrane was captured directly by an optical microscope after stabilizing for 2 h. Afterward, the electrolyte was alternatively replaced with 0.5 or 0.8 or 1.0 M NaCl solution to observe the thickness change. The average interlayer spacing (d_{ave}) of solvated GO membrane was estimated by multiplying the interlayer spacing (d) of the dry GO membrane (0.75 nm probed by XRD) with the relative ratio of the thickness (t) of solvated GO membrane to that of dry membrane:

$$d_{ave} \text{ (solvated GO membrane)} = \frac{d \text{ (dry GO membrane)} \times t \text{ (solvated GO membrane)}}{t \text{ (dry GO membrane)}} \quad (1)$$

Average interlayer spacing of rGO (d_{ave}) membrane was calculated with the assumption from the conventional structure model that the nanosheet was evenly distributed along the stacking direction^[4]

$$d_{ave} = \frac{\text{Area density of graphene}}{\text{Density of rGO membrane}} \quad (2)$$

where the area density of graphene was 0.77 mg cm^{-2} .^[4]

The packing density of the membrane was measured by the ratio of mass to volume. Specifically, the mass of a single membrane was obtained by averaging the mass of four pieces of membranes (diameter of 0.6 cm), which were probed by the balance (HR-250AZ). The volume was calculated based on the diameters (0.6 cm) and thickness of the sample, which was averaged by four pieces of membranes with three measurements on each sample (probed by an RS PRO micrometer).

Small-Angle X-ray Scattering: The SAXS data was collected under an ambient condition at the SAXS/WAXS beamline at the Australia Synchrotron, Melbourne, Australia. The measurement was conducted in the transmission mode with the incident beam perpendicularly passing through the membrane plane (through the surface) and through the cross-section plane (through the edge), respectively. In these measurements, the energy of the incident X-ray beam was set at i) 20 keV ($\lambda = 0.620 \text{ \AA}$) at the camera length of 746 mm and ii) 8.2 keV ($\lambda = 1.512 \text{ \AA}$) at the camera length of 7396 mm, separately to yield a total scatter wave vector (q) in the range from $2 \times 10^{-3} \text{ \AA}^{-1}$ to 2 \AA^{-1} , which was defined as

$$q = 4\pi \sin\left(\frac{\theta}{\lambda}\right) \quad (3)$$

where 2θ is the scattering angle and λ is the wavelength of the X-ray.

Orientation distribution coefficient, S , introduced by Hermans^[25] was used to estimate the degree of orientation of aligned nanosheets, for which $S = 1$ and -0.5 means perfect orientation along the $\varphi = 0^\circ$ and 90° direction, respectively, and $S = 0$ means completely random orientation.

$$S = \frac{1}{2} (3 \langle \cos^2 \varphi \rangle - 1) \quad (4)$$

where $\langle \cos^2 \varphi \rangle$ is the average cosine square weighted by the azimuthal intensity $I(\varphi)$, which can be calculated by

$$\langle \cos^2 \varphi \rangle = \frac{\int_0^{2\pi} I(\varphi) \cos^2 \varphi \sin \varphi \, d\varphi}{\int_0^{2\pi} I(\varphi) \sin \varphi \, d\varphi} \quad (5)$$

The reduction of the 2D scattering pattern to the 1D scattering curve and the relevant data processing was performed by scatterbrain (V2.82) and Irena/Nika package (V2.7) under IgorPro8 environment.^[38]

Stacking Structure of rGO Membrane: The microstructure was probed by a Helium Ion Microscope (Zeiss ORION NanoFab). XRD was used to probe the crystallized structure in graphene membrane on Bruker D8 Advance with Cu K α radiation ($\lambda = 1.54 \text{ \AA}$). The measurement was taken at a range of 5° to 35° . The data analysis of XRD spectra was following Manoj's work^[22] to extrapolate the crystalline carbon and amorphous carbon in graphene membrane and to describe the structural features in terms of the stacking height (L_c)^[39] and interlayer spacing (d) calculated by the following equations.

$$L_c = \frac{0.89\lambda}{FWHM(2\theta) \cos \theta} \quad (6)$$

$$d = \frac{\lambda}{2 \sin \theta} \quad (7)$$

where $FWHM(2\theta)$ represents the full width of half maximum of the peaks.

Renishaw inVia Raman Microscope was applied to probe the structural units in the graphene membrane using 532 nm laser excitation at room temperature with a laser power of 1 mW. The analysis of the Raman data was based on the work done by Claramunt^[40] and Malard.^[41] Specifically, four Lorentzian functions were used to fit I ($\approx 1180 \text{ cm}^{-1}$), D ($\approx 1350 \text{ cm}^{-1}$), G ($\approx 1590 \text{ cm}^{-1}$), D' ($\approx 1620 \text{ cm}^{-1}$) peak separately, and one additional Gaussian function was used to fit D'' peak ($\approx 1490 \text{ cm}^{-1}$) for the first order. Three Lorentzian functions were used to fit D + I ($\approx 2480 \text{ cm}^{-1}$), 2D ($\approx 2680 \text{ cm}^{-1}$) and D + G ($\approx 2920 \text{ cm}^{-1}$) peak, plus one Gaussian function used for fitting 2D' and G + D' ($\approx 3200 \text{ cm}^{-1}$) peak. The ratio of intensity of D (I_D) to intensity of G (I_G) can be used to estimate the size of the graphitized domain L_a . It needs to be careful that L_a was defined as the length of the aromatic domain in a single nanosheet instead of the lateral size of a stacked graphitized cluster.^[42] TK model was only applicable for $4 \text{ nm} < L_a < 10 \text{ nm}$. For these cases, the Lucchese model ($L_a < 4 \text{ nm}$) was alternatively more accurate for calculating the graphitized domain size.^[40] Here, the Lucchese equation is used to calculate L_a

$$\frac{I_D}{I_G} = C_A \frac{(r_A^2 - r_s^2)}{(r_A^2 - 2r_s^2)} \left[\exp\left(-\pi \frac{r_s^2}{L_a^2}\right) - \exp\left(-\pi \frac{(r_A^2 - r_s^2)}{L_a^2}\right) \right] \quad (8)$$

From which, $C_A = 5.43$ for 532 nm laser, $r_A = 3.1 \text{ nm}$, $r_s = 1.0 \text{ nm}$.

Electrochemical Characterization: Electro sorption measurement was conducted following the work done by Zhu et al. and Yang et al.^[4,21a] The principle of this method was inferring the pore structure by measuring ion transport behavior. For example, i) higher overall capacitance indicates the higher accessible area to ions; ii) the dynamic ion resistance will help to deduce the pore connectivity and other factors affecting the ion transfer resistivity. Unlike the BET method, which uses inert gas as penetration media, this method was a powerful technique using ions that had tailorable size and affinity, and the penetration problem will be minimized. For this measurement, two graphene membranes need to be assembled into a symmetric two-electrode configuration. Before assembling, the graphene membranes were first immersed in 1.0 M H₂SO₄ overnight. The membrane was placed on the current collector made by Pt foil. The current collector connects to a platinum wire which had been connected to a multi-channel electrochemical state for the measurement. A glass fiber soaked in 1.0 M H₂SO₄ was settled between two graphene membranes as the separator. CV scanning

was first measured ten times for each rate from 5 to 500 mV s⁻¹. The data was only collected from the last running of every rate to make sure the data collected was at a stable state. Then the electrochemical impedance spectroscopy (EIS) was conducted at the frequency ranges from 100 MHz to 200 kHz at the signal amplitude of 10 mV. Finally, the galvanostatic charge–discharge test was carried out at different charging rates from 1.0 to 150 A g⁻¹ under a limited operation voltage of 1.0 V.

Supporting Information

Supporting Information is available from the Wiley Online Library or from the author.

Acknowledgements

D.L. is grateful for the financial support from the Australian Research Council (FL180100029 and DP180102890) and the University of Melbourne. The authors thank the Australian Synchrotron for support on the Small/Wide X-ray scattering instrument through proposal M14459 and M17715. The authors acknowledge the use of the facilities with the help of Dr. Anders Barlow from the Materials Characterization and Fabrication Platform at the University of Melbourne and the use of facilities in Monash X-ray Platform from Monash University. The authors thank Dr. Qinghua Liang and Dr. Wenjie Jiang for their helpful discussion.

Open access publishing facilitated by The University of Melbourne, as part of the Wiley - The University of Melbourne agreement via the Council of Australian University Librarians.

Conflict of Interest

The authors declare no conflict of interest.

Data Availability Statement

The data that support the findings of this study are available from the corresponding author upon reasonable request.

Keywords

2D assemblies, 2D laminar membrane structures, ion transportation pathways, reduced graphene oxide membranes, supercapacitors

Received: February 7, 2022

Revised: March 13, 2022

Published online:

- [1] a) J. Luo, L. J. Cote, V. C. Tung, A. T. Tan, P. E. Goins, J. Wu, J. Huang, *J. Am. Chem. Soc.* **2010**, *132*, 17667; b) J. L. Feng, Y. Q. Ye, M. Xiao, G. Wu, Y. Ke, *Chem. Pap.* **2020**, *74*, 3767; c) S. F. Pei, H. M. Cheng, *Carbon* **2012**, *50*, 3210.
- [2] a) C. Mattevi, G. Eda, S. Agnoli, S. Miller, K. A. Mkhoyan, O. Celik, D. Mastrogiovanni, G. Granozzi, E. Garfunkel, M. Chhowalla, *Adv. Funct. Mater.* **2009**, *19*, 2577; b) A. Akbari, B. V. Cunnings, S. R. Joshi, C. H. Wang, D. C. Camacho-Mojica, S. Chatterjee, V. Modepalli, C. Cahoon, C. W. Bielawski, P. Bakharev, G. H. Kim, R. S. Ruoff, *Matter* **2020**, *2*, 1198.
- [3] a) P. Huang, Y. Li, G. Yang, Z.-X. Li, Y.-Q. Li, N. Hu, S.-Y. Fu, K. S. Novoselov, *Nano Mater. Sci.* **2021**, *3*, 1; b) G. Liu, W. Jin, N. Xu,

Chem. Soc. Rev. **2015**, *44*, 5016; c) S. J. Wan, L. Jiang, Q. F. Cheng, *Matter* **2020**, *3*, 696.

- [4] X. Yang, C. Cheng, Y. Wang, L. Qiu, D. Li, *Science* **2013**, *341*, 534.
- [5] a) B. Qi, X. He, G. Zeng, Y. Pan, G. Li, G. Liu, Y. Zhang, W. Chen, Y. Sun, *Nat. Commun.* **2017**, *8*, 825; b) J. Abraham, K. S. Vasu, C. D. Williams, K. Gopinadhan, Y. Su, C. T. Cheria, J. Dix, E. Prestat, S. J. Haigh, I. V. Grigorieva, P. Carbone, A. K. Geim, R. R. Nair, *Nat. Nanotechnol.* **2017**, *12*, 546.
- [6] Z. Li, S. Gadipelli, H. Li, C. A. Howard, D. J. L. Brett, P. R. Shearing, Z. Guo, I. P. Parkin, F. Li, *Nat. Energy* **2020**, *5*, 160.
- [7] a) Y. Wen, M. Wu, M. Zhang, C. Li, G. Shi, *Adv. Mater.* **2017**, *29*, 1702831; b) X. J. Chen, X. M. Deng, N. Y. Kim, Y. Wang, Y. Huang, L. Peng, M. Huang, X. Zhang, X. Chen, D. Luo, B. Wang, X. Z. Wu, Y. F. Ma, Z. Lee, R. S. Ruoff, *Carbon* **2018**, *132*, 294; c) Z. Xu, Y. Liu, X. Zhao, L. Peng, H. Sun, Y. Xu, X. Ren, C. Jin, P. Xu, M. Wang, C. Gao, *Adv. Mater.* **2016**, *28*, 6449.
- [8] D. Li, M. B. Muller, S. Gilje, R. B. Kaner, G. G. Wallace, *Nat. Nanotechnol.* **2008**, *3*, 101.
- [9] a) L. Qiu, X. Zhang, W. Yang, Y. Wang, G. P. Simon, D. Li, *Chem. Commun.* **2011**, *47*, 5810; b) A. Sinititskii, D. V. Kosynkin, A. Dimiev, J. M. Tour, *ACS Nano* **2010**, *4*, 3095; c) Y. Wang, X. Zhang, D. Li, *Chem. Commun.* **2015**, *51*, 17760.
- [10] a) S. H. Huh, in *Phys. Appl. Graphene: Exp.* (Ed: S. Mikhailov), IntechOpen, London, English **2011**, Ch. 5; b) M. F. El-Kady, V. Strong, S. Dubin, R. B. Kaner, *Science* **2012**, *335*, 1326.
- [11] a) T. Kim, G. Jung, S. Yoo, K. S. Suh, R. S. Ruoff, *ACS Nano* **2013**, *7*, 6899; b) X. Chen, W. Li, D. Luo, M. Huang, X. Wu, Y. Huang, S. H. Lee, X. Chen, R. S. Ruoff, *ACS Nano* **2017**, *11*, 665.
- [12] I. K. Moon, J. Lee, R. S. Ruoff, H. Lee, *Nat. Commun.* **2010**, *1*, 73.
- [13] Y. Su, V. G. Kravets, S. L. Wong, J. Waters, A. K. Geim, R. R. Nair, *Nat. Commun.* **2014**, *5*, 4843.
- [14] a) A. Mahmood, Z. Yuan, X. Sui, M. A. Riaz, Z. Yu, C. Liu, J. Chen, C. Wang, S. Zhao, N. Mahmood, Z. Pei, L. Wei, Y. Chen, *Energy Storage Mater.* **2021**, *41*, 395; b) T. Foller, R. Daiyan, X. Jin, J. Leverett, H. Kim, R. Webster, J. E. Yap, X. Wen, A. A. Rawal, *Mater. Today* **2021**, *50*, 44.
- [15] A. G. Pandolfo, A. F. Hollenkamp, *J. Power Sources* **2006**, *157*, 11.
- [16] a) M. Salanne, B. Rotenberg, K. Naoi, K. Kaneko, P. L. Taberna, C. P. Grey, B. Dunn, P. Simon, *Nat. Energy* **2016**, *1*, 16070; b) Y. L. Qian, X. L. Zhang, C. Y. Liu, C. Zhou, A. S. Huang, *Desalination* **2019**, *460*, 56.
- [17] H. Sun, L. Mei, J. Liang, Z. Zhao, C. Lee, H. Fei, M. Ding, J. Lau, M. Li, C. Wang, X. Xu, G. Hao, B. Papandrea, I. Shakir, B. Dunn, Y. Huang, X. Duan, *Science* **2017**, *356*, 599.
- [18] a) J. Xu, Z. Q. Tan, W. C. Zeng, G. X. Chen, S. L. Wu, Y. Zhao, K. Ni, Z. C. Tao, M. Ikram, H. X. Ji, Y. W. Zhu, *Adv. Mater.* **2016**, *28*, 5222; b) Y. J. Zhao, J. H. He, *Carbon* **2021**, *178*, 734; c) J. Kim, J. H. Eum, J. Kang, O. Kwon, H. Kim, D. W. Kim, *Sci. Rep.* **2021**, *11*, 2063.
- [19] C. N. Yeh, K. Raidongia, J. Shao, Q. H. Yang, J. Huang, *Nat. Chem.* **2014**, *7*, 166.
- [20] X. Yang, J. Zhu, L. Qiu, D. Li, *Adv. Mater.* **2011**, *23*, 2833.
- [21] a) J. Zhu, C. Cheng, X. Yang, Y. Wang, L. Qiu, D. Li, *Chem. - Eur. J.* **2013**, *19*, 3082; b) C. Cheng, J. Zhu, X. Yang, L. Qiu, Y. Wang, D. Li, *J. Mater. Chem. A* **2013**, *1*, 9332.
- [22] B. Manoj, *Int. J. Miner. Metall. Mater.* **2014**, *21*, 940.
- [23] a) C. D. Wood, M. J. Palmeri, K. W. Putz, Z. An, S. T. Nguyen, L. C. Brinson, *J. Appl. Mech.* **2013**, *80*, 040913; b) S. Wang, J. Lin, Z. Xu, Z. Xu, *Composites, Part A* **2021**, *143*, 106318; c) K. W. Putz, O. C. Compton, C. Segar, Z. An, S. T. Nguyen, L. C. Brinson, *ACS Nano* **2011**, *5*, 6601.
- [24] a) T. F. Yen, J. G. Erdman, S. S. Pollack, *Anal. Chem.* **2002**, *33*, 1587; b) L. Lu, V. Sahajwalla, C. Kong, D. Harris, *Carbon* **2001**, *39*, 1821.
- [25] J. J. Hermans, P. H. Hermans, D. Vermaas, A. Weidinger, *Recl. Trav. Chim. Pays-Bas* **1946**, *65*, 427.
- [26] a) P. W. Schmidt, *J. Appl. Crystallogr.* **1991**, *24*, 414; b) H. D. Bale, P. W. Schmidt, *Phys. Rev. Lett.* **1984**, *53*, 596.

- [27] Y. Yang, Y. C. Zou, C. R. Woods, Y. Shi, J. Yin, S. Xu, S. Ozdemir, T. Taniguchi, K. Watanabe, A. K. Geim, K. S. Novoselov, S. J. Haigh, A. Mishchenko, *Nano Lett.* **2019**, *19*, 8526.
- [28] K. Raidongia, J. Huang, *J. Am. Chem. Soc.* **2012**, *134*, 16528.
- [29] K. Norrish, *Discuss. Faraday Soc.* **1954**, *18*, 120.
- [30] A. Boretti, S. Al-Zubaidy, M. Vaclavikova, M. Al-Abri, S. Castelletto, S. Mikhalovsky, *npj Clean Water* **2018**, *1*, 5.
- [31] L. Chen, G. Shi, J. Shen, B. Peng, B. Zhang, Y. Wang, F. Bian, J. Wang, D. Li, Z. Qian, G. Xu, G. Liu, J. Zeng, L. Zhang, Y. Yang, G. Zhou, M. Wu, W. Jin, J. Li, H. Fang, *Nature* **2017**, *550*, 380.
- [32] D. Jang, J. C. Idrobo, T. Laoui, R. Karnik, *ACS Nano* **2017**, *11*, 10042.
- [33] Z. J. He, Z. Qi, H. C. Liu, K. Y. Wang, L. Roberts, J. Z. Liu, Y. L. Liu, S. J. Wang, M. J. Cook, G. P. Simon, L. Qiu, D. Li, *Natl. Sci. Rev.* **2021**, <https://doi.org/10.1093/nsr/nwab184>.
- [34] a) Y. Xu, Z. Lin, X. Zhong, X. Huang, N. O. Weiss, Y. Huang, X. Duan, *Nat. Commun.* **2014**, *5*, 4554; b) Y. Li, W. Zhao, M. Weyland, S. Yuan, Y. Xia, H. Liu, M. Jian, J. Yang, C. D. Easton, C. Selomulya, X. Zhang, *Environ. Sci. Technol.* **2019**, *53*, 8314.
- [35] Y. Tao, X. Xie, W. Lv, D. M. Tang, D. Kong, Z. Huang, H. Nishihara, T. Ishii, B. Li, D. Golberg, F. Kang, T. Kyotani, Q. H. Yang, *Sci. Rep.* **2013**, *3*, 2975.
- [36] a) T.-T. Nguyen, A. Demortière, B. Fleutot, B. Delobel, C. Delacourt, S. J. Cooper, *npj Comput. Mater.* **2020**, *6*, 123; b) S. J. Cooper, A. Bertei, P. R. Shearing, J. A. Kilner, N. P. Brandon, *SoftwareX* **2016**, *5*, 203.
- [37] W. S. Hummers, R. E. Offeman, *J. Am. Chem. Soc.* **1958**, *80*, 1339.
- [38] a) J. Ilavsky, *J. Appl. Crystallogr.* **2012**, *45*, 324; b) J. Ilavsky, P. R. Jemian, *J. Appl. Crystallogr.* **2009**, *42*, 347.
- [39] J. Lin, Z. Peng, Y. Liu, F. Ruiz-Zepeda, R. Ye, E. L. Samuel, M. J. Yacaman, B. I. Yakobson, J. M. Tour, *Nat. Commun.* **2014**, *5*, 5714.
- [40] S. Claramunt, A. Varea, D. Lopez-Diaz, M. M. Velazquez, A. Cornet, A. Cirera, *J. Phys. Chem. C* **2015**, *119*, 10123.
- [41] L. M. Malard, M. A. Pimenta, G. Dresselhaus, M. S. Dresselhaus, *Phys. Rep.* **2009**, *473*, 51.
- [42] M. M. Lucchese, F. Stavale, E. H. M. Ferreira, C. Vilani, M. V. O. Moutinho, R. B. Capaz, C. A. Achete, A. Jorio, *Carbon* **2010**, *48*, 1592.